

# Turbulent mixing in a stratified fluid

Joanne M. Holford <sup>\*</sup>, P.F. Linden <sup>1</sup>

*Department of Applied Mathematics and Theoretical Physics, University of Cambridge, Silver Street,  
Cambridge, England CB3 9EW, UK*

Received 22 September 1998; received in revised form 10 May 1999; accepted 28 June 1999

---

## Abstract

The strength of diapycnal mixing by small-scale motions in a stratified fluid is investigated through changes to the mean buoyancy profile. We study the mixing in laboratory experiments in which an initially linearly stratified fluid is stirred with a rake of vertical bars. The flow evolution depends on the Richardson number ( $Ri$ ), defined as the ratio of buoyancy forces to inertial forces. At low  $Ri$ , the buoyancy flux is a function of the local buoyancy gradient only, and may be modelled as gradient diffusion with a  $Ri$ -dependent eddy diffusivity. At high  $Ri$ , vertical vorticity shed in the wakes of the bars interacts with the stratification and produces well-mixed layers separated by interfaces. This process leads to layers with a thickness proportional to the ratio of grid velocity to buoyancy frequency for a wide range of Reynolds numbers ( $Re$ ) and grid solidities. In this regime, the buoyancy flux is not a function of the local gradient alone, but also depends on the local structure of the buoyancy profile. Consequently, the layers are not formed by the Phillips/Posmentier mechanism, and we show that they result from vortical mixing previously thought to occur only at low  $Re$ . The initial mixing efficiency shows a maximum at a critical  $Ri$  which separates the two classes of behaviour. The mixing efficiency falls as the fluid mixes and as the layered structure intensifies and, therefore, the mixing efficiency depends not only on the overall  $Ri$ , but also on the dynamics of the structure in the buoyancy field. We discuss some implications of these results to the atmosphere and oceans. © 1999 Elsevier Science B.V. All rights reserved.

**Keywords:** Turbulent mixing; Stratified fluid; Buoyancy

---

---

<sup>\*</sup> Corresponding author. Tel.: +44-1223-337858; fax: +44-1223-337918

<sup>1</sup> Present address: Department of Mechanical and Aerospace Engineering, University of California, San Diego, 9500 Gilman Drive, La Jolla, CA 92093-0411, USA.

## 1. Introduction

In nature, most fluids are perturbed by motions on a wide range of scales. While systematic flows on larger scales can be calculated directly, smaller turbulent motions occur below the resolution of most numerical models. These small-scale motions are important, both as a sink of large-scale energy and through enhanced transport of passive scalars, buoyancy and momentum. In this study, the transport of buoyancy in a particular turbulent field in a stratified fluid is investigated.

In an unstratified turbulent fluid, the mean flux  $\mathbf{q}_s$  of a passive scalar  $s$  is proportional to the mean concentration gradient,  $\mathbf{q}_s = -K_s \nabla s$ , for times large compared to the Lagrangian timescale of the turbulence (Taylor (1915); Batchelor (1949)). The constant of proportionality,  $K_s$ , known as the eddy diffusivity, can be expressed in terms of the time rate of change of root mean square (rms) particle displacements and, in homogeneous isotropic turbulence, is approximately equal to the product of the turbulent integral lengthscale and the rms turbulent velocity.

Stable stratification affects the flow in several ways. Vertical mixing of the stratification provides an additional sink of energy. The stratification also influences the structure of the turbulence, since vertical motions are directly affected by buoyancy forces. Turbulence in a stratified fluid is typically anisotropic, with reduced vertical velocities and vertical lengthscales, and a reduced correlation between the density perturbation and the vertical velocity component, as seen, for example, in the stratified flume experiments of Stillinger et al. (1983). Horizontal motions organise into vortical structures, which then cascade energy to larger scales. The experiments of Fincham et al. (1994), in which the decaying wake behind a rake of vertical bars towed once through a stratified fluid was observed, exemplify this flow regime, which is ultimately dominated by an interacting field of large aspect ratio “pancake” vortices at different levels.

The concept of turbulent gradient diffusion may be extended to weakly stratified fluids by allowing the eddy diffusivity to vary with the local buoyancy gradient  $N^2$ . For example, Noh and Fernando (1995) use an eddy diffusivity based on the local turbulent kinetic energy (TKE)  $e$ , and a vertical mixing length which varies with local Richardson number,  $Ri$ , taking the values  $l_0$  in an unstratified fluid and  $e^{1/2}/N$  in a strongly stratified fluid.

An overall measure of the mixing in a flow is the mixing efficiency  $\eta$ , here defined as the ratio of the change in background potential energy ( $\overline{PE}$ ) of the fluid to the change in available (potential and kinetic) energy. The mixing efficiency lies in the range  $0 \leq \eta \leq 1$ , and all input energy not absorbed doing work against gravity is removed by viscous dissipation. The average stability of the flow can be measured by an overall or bulk  $Ri$ ,  $Ri_b$ , as defined, for example, by Turner (1973), p. 12, and a relationship between  $\eta$  and  $Ri_b$  is useful for parametrisations of mixing. In the limit of weak stratification, when density behaves as a passive tracer,  $\eta$  increases linearly with  $Ri_b$ . At higher  $Ri_b$ , a variety of experiments drawn together by Linden (1979) show that the mixing efficiency may reach a peak and then decrease with increasing  $Ri_b$ , as the character of the perturbing flow is altered by buoyancy effects.

A common feature of strongly stratified flows, e.g., Dalaudier et al. (1994), is the presence of persistent small-scale structure in the stratification. Phillips (1972) and

independently Posmentier (1977) showed that if the buoyancy flux was a decreasing function of the local buoyancy gradient, a fine structure of layers and interfaces develops spontaneously in the buoyancy profile. Both authors recognised that their model was not valid at scales smaller than the turbulent scale, and that some form of averaging was required. Barenblatt et al. (1993) proposed the addition of a time delay in the response of the turbulence to stratification changes, to address this question and developed a well-posed model that generates layers. The model of Balmforth et al. (1997), which allows the TKE density to vary in time with the evolving flow, also generates layers through a related mechanism which depends crucially on the parametrisation of the stirring process.

In the laboratory, the development of layers in an evenly stirred, linearly stratified fluid has been observed under a variety of stirring configurations, in the experiments of Ruddick et al. (1989) and Park et al. (1994) (hereafter referred to as PWG94). In the latter work, a layer scale related to the stirring velocity and the buoyancy gradient was identified. A stirring mechanism with no vertical structure, such as a towed or oscillated vertical bar, was chosen for these experiments, in contrast to the experiments of Liu (1995) in which a biplanar grid was towed to generate layers on the scale of the grid. PWG94 suggested that the generation of a layered structure in their experiments was clear proof of the Phillips/Posmentier mechanism, although they did not attempt to determine the relationship between buoyancy flux and gradient. They showed that the mixing efficiency typically decreased with time, and that when only two layers remained, the mixing efficiency was a decreasing function of interfacial  $Ri$ .

A study at lower Reynolds numbers ( $Re$ ), by Holford and Linden (1999a), observed layering in a fluid stirred by a towed vertical rake, caused by the interaction between coherent centres of vertical vorticity in the wake and the background stratification. Vertical mixing is enhanced where the vortices are tilted away from the vertical, and suppressed at the limits of the vortex perturbations, where the vorticity remains vertical. This vertical inhomogeneity of mixing leads to the development of layers and interfaces in the stratification. The observed distortion of the vortex cores is similar to that predicted by the theoretical model of Majda and Grote (1997), and may be related to the instability involving a resonance of inertial waves in the vortex core and internal waves identified by Miyazaki and Fukumoto (1992). The question arises as to whether this mechanism operates at higher  $Re$  when the vortices shed from the rake are turbulent.

In the above experiments, a layered structure develops from an initially linear profile. Once layers are formed further mixing may be controlled by the rates of mixing across the interfaces between them. The mixing at interfaces has been studied in “mixing box” experiments, e.g., Turner (1968), in which a horizontal biplanar grid is oscillated to generate the turbulence. The mixing is characterised by an entrainment velocity, proportional to the ratio of buoyancy flux to buoyancy jump across the interface, and is found to scale on the local  $Ri$  as  $Ri^{-n}$ . From the review of Fernando (1991), the general consensus is that  $n$  satisfies  $n > 1$ , in which case the buoyancy flux at the interface is a decreasing function of the local  $Ri$ .

In this study, laboratory experiments were carried out to examine the changes in flow structure and mixing efficiency with  $Ri$ , over a wide range of  $Re$ . An initially linear stratification was stirred repeatedly with a rake of vertical square bars. Experiments were

carried out both in a tank at DAMTP, at grid  $Re$  of about 500, and in a much larger tank at the Environmental Flow Research Laboratory (EnFlo) at the University of Surrey, where grid  $Re$  of the order of 4000 were attained.

The details of the experiments are given in Section 2, with a discussion of the technique for measuring the buoyancy profiles of the evolving flow. At low  $Ri$ , the mean buoyancy field evolves as if under an enhanced diffusivity, which varies with  $Ri$ , and is discussed in Section 3. At higher  $Ri$ , the buoyancy field no longer evolves smoothly, but develops into a series of well-mixed layers separated by sharp interfaces. In Section 4, the mechanism of layer formation at high  $Ri$  is investigated, and the variation of buoyancy flux and mixing efficiency with initial  $Ri$  and with time is investigated. It is shown that the buoyancy flux is not a function of the density gradient and so the Phillips/Posmentier mechanism is not the cause of the layering. Instead, we show that the layers are produced by the distortion of vortical motions even at high  $Re$ . The conclusions and the implications for the oceans and atmosphere are given in Section 5.

2. Experimental apparatus and measurement techniques

2.1. The experiments

Experiments were carried out in two rectangular tanks, width  $W$ , in fluid of depth  $H$ . For the tank at DAMTP,  $W = 25.6$  cm and  $H \lesssim 50$  cm, while for the tank at EnFlo,  $W = 125$  cm and  $H \lesssim 80$  cm. On both tanks, a carriage was moved from end to end at a constant velocity  $U$ , except for small regions of acceleration and deceleration. Velocities in the range  $1.0 \text{ cm s}^{-1} < U < 7.0 \text{ cm s}^{-1}$  were used in both facilities. A rake of bars was mounted vertically below the carriage, aligned across the tank. False walls allowed the length  $L$  of the working volume of the fluid to be varied, and ensured that the rake motion spanned the whole working length. The range of grid geometries and tank lengths used are given in Table 1, together with the symbol used to represent each set of

Table 1  
The six grid geometries used in these experiments. Experiments with grids A to E were carried out at DAMTP, and experiments with grid F were carried out at EnFlo. Note that A and F are directly comparable with the same geometry at two different scales

	$d$ (cm)	$M$ (cm)	$S$	$n_{\text{bars}}$	$L$	Symbol
A	0.65	3.25	0.20	8	$5\text{--}20M$	■
B	0.65	6.50	0.10	4	$6M$	●
C	2.50	6.40	0.39	4	$8M$	◇
D	2.50	12.80	0.20	2	$4M$	□
E	2.80	25.60	0.11	1	$2.5M$	○
F	3.15	15.60	0.20	8	$25M$	*

experiments in subsequent figures. Here,  $d$  is the width of the bars, and  $M$  is the bar spacing, giving a grid solidity of  $S = d/M$ . The distance the rake was towed on each stir is  $L_{\text{stir}} \approx L - M$ .

All experiments were set up with an approximately linear salt stratification, produced either by the double-bucket method or through a mixing valve, from salt water and fresh water reservoirs. The buoyancy frequency range used was  $0.4 \text{ s}^{-1} < N < 2.2 \text{ s}^{-1}$ . At EnFlo, the reuse of saline water allowed it to become several degrees warmer than the fresh water (which was stored outdoors), creating sharp double-diffusive layers in the tank, on a scale of about 1 cm. Before each experiment, this fine structure was removed by several stirs with the rake. At DAMTP, the temperatures of both fluid reservoirs and the laboratory were always within  $1^\circ\text{C}$ , and no double-diffusive effects were seen.

Each experiment consisted of a sequence of  $n_{\text{stirs}}$  single stirs of the rake from one end of the tank to the other, with little pause between successive stirs. The (constant) grid velocity is denoted by  $U$ , and the total stirring time in each sequence is then  $T = n_{\text{stirs}} L_{\text{stir}}/U$ . At the end of each sequence, transient motions were allowed to decay for 150 s and the mean density profile was measured from a downward traverse of a suction-type conductivity probe. This time delay was chosen to allow transient motions to decay, while capturing the sharp features of the density interfaces. Most of the density measurements presented here are from experiments in DAMTP, and this measurement system is described in Section 2.2. A similar measurement system was used at EnFlo. In addition, the evolving density field was observed using a shadowgraph, which shows regions of nonzero density curvature. These images allow the layer scales to be determined independently of density profiles, and reveal details of the transient flow structures.

## 2.2. Measurement of density profiles

The conductivity probe was mounted on a vertical traverse driven by a servo motor with a position-resolving potentiometer. The probe was traversed downwards at  $1.3 \text{ cm s}^{-1}$  and the conductivity and vertical position were logged by computer at a frequency of  $20 \text{ s}^{-1}$ , via a CUBAN-12B analogue to digital converter (ADC). The main uncertainty in the position measurement was the offset from the base of the tank, as the probe was moved and repositioned for each sequence of stirs, in order to allow the rake to stir the whole working volume of fluid. This uncertainty was estimated at  $\pm 5 \times 10^{-2} \text{ cm}$ , whereas within each traverse the relative position was accurate to  $\pm 1 \times 10^{-2} \text{ cm}$ .

The conductivity probe was connected to a Cambustion Multichannel Conductivity Meter MCM10A, and calibrated at least every five experiments, using 10 test salt solutions, the densities of which were measured with a Stanton Redcroft PAAR DMA 60/602 density meter. The calibration took the form of  $\rho = \rho_{\text{max}} - k\sqrt{V_{\text{max}} - V}$ , where  $k$  is a constant,  $\rho_{\text{max}}$  is the density of saturated salt solution, and the measured voltage,  $V$ , is proportional to the conductance of the fluid. The estimated error in the density measurement, based on the resolution of the ADC, is  $\pm 5 \times 10^{-5} \text{ g cm}^{-3}$ . The probe calibration drifted by less than  $10^{-4} \text{ g cm}^{-3} \text{ day}^{-1}$  which, over the course of an experiment, is less than the resolution of the system. Density measurement errors of up

to  $3.2 \times 10^{-4} \text{ g cm}^{-3}$  may result from conductivity changes caused by changes in the bulk fluid temperature. Since these are uniform throughout the tank, they do not contribute to errors in the density gradient. The volume flow rate of the probe is  $5 \times 10^{-2} \text{ cm}^3 \text{ s}^{-1}$ , and a (negligible)  $2.5 \text{ cm}^3$  of fluid is extracted in each probe traverse. The flushing frequency of the probe tip of  $160 \text{ s}^{-1}$  is much higher than the measurement frequency.

The probe traverse extended to within 5 mm of the top and bottom boundaries of the fluid, and the raw density data is first extrapolated to the boundaries, using functions which enforce the condition  $\partial\rho/\partial z = 0$  at the impermeable surfaces. The extrapolation was least successful for the initial density profile, which is controlled by molecular diffusion, and the first stirring sequence was often excluded from subsequent processing. Then the data are interpolated onto a regular grid of 0.1 cm spacing, using Gaussian weighting with a lengthscale of 0.2 cm. Each profile is corrected by the addition of a uniform density, to ensure that the measured mass of fluid remains constant. Departures from mass conservation in the raw data are typically 0.05% over the course of an experiment, and are due to a combination of several effects, including slight differences between the vertical offset of the probe in each sequence, the withdrawal of fluid through the probe, evaporation, temperature changes affecting the conductivity measurement and possibly deviations from horizontal homogeneity in the measured fluid. Finally, the data was low pass filtered in time before calculating the buoyancy flux by finite differences.

### 2.3. Quantities calculated from density profiles

The density measurements give a sequence of profiles  $\rho_n(z)$ , at the end of the  $n$ th stirring sequence. The density will be discussed in terms of the buoyancy:

$$b = - \frac{g(\rho - \rho_0)}{\rho_0}, \quad (2.1)$$

where  $\rho_0$  is the mean density of the fluid and  $g$  is the acceleration due to gravity. The buoyancy frequency  $N = (\partial b / \partial z)^{1/2}$ , where  $z$  is the vertical coordinate (positive upwards). The flux  $\mathbf{q}$  of buoyancy is defined through the flux equation:

$$\frac{\partial b}{\partial t} = - \nabla \cdot \mathbf{q}, \quad (2.2)$$

and the flux conditions at all boundaries of the fluid. The instantaneous turbulent field has considerable structure, and the associated buoyancy flux is a complex function of space and time. Here, however, we are examining the mean buoyancy flux over each sequence of stirs. Since the measured buoyancy field is approximately horizontally homogeneous, the buoyancy flux associated with the changing profile is  $\mathbf{q} = q(z, t)\hat{\mathbf{z}}$ . The mean buoyancy flux during sequence  $n$  is calculated by:

$$q_n(z) = - \frac{1}{T} \int_0^z \{b_n(z') - b_{n-1}(z')\} dz',$$

where it is assumed that  $q_n(0) = 0$ . The requirement that mass is conserved ensures that  $q_n(H) = 0$  also.

The buoyancy flux is a local measure of the mixing at any level in the fluid. A useful overall measure of the mixing is the mixing efficiency,  $\eta$ , which in its most general form can be defined between two times as:

$$\eta = \frac{\Delta \overline{PE}}{(\Delta \overline{PE} - \Delta E)}, \quad (2.3)$$

where  $\Delta \overline{PE}$  is the change in background potential energy and  $\Delta E$  is the change in the total energy of the fluid. The background PE is the potential energy of the density distribution formed by reordering all density elements, see Winters et al. (1995). This definition gives a time-dependent mixing efficiency which satisfies  $0 \leq \eta \leq 1$ . In the present experiments,  $\eta$  is calculated for each stirring sequence, over which  $\Delta \overline{PE} - \Delta E = -\Delta KE$ , assuming that all the energy put in by the rake is kinetic energy (KE). The reduction in KE over a stirring sequence is equal to the KE imparted by the rake, giving:

$$-\Delta KE = n_{\text{bars}} H n_{\text{stirs}} L_{\text{stir}} \frac{1}{2} C_d \rho_0 d U_0^2, \quad (2.4)$$

where  $C_d$  is the drag coefficient for a single bar. Numerical calculations of two-dimensional flow around a square cylinder, by Davis and Moore (1982), suggest that the drag coefficient increases with  $Re_d$ , the  $Re$  based on the bar width, in the range  $200 < Re_d < 2000$ . We have approximated this relationship as  $C_d = 0.57 + 0.50 \log Re_d$ . In Eq. (2.4), the drag force is estimated using the velocity  $U_0 = U/(1 - S)$ , the difference between the velocity of the bars and the velocity of a uniform return flow between the bars. This velocity difference is the most appropriate scale to account for variations in drag with grid solidity  $S$ . Numerical results of two-dimensional flow around a circular bar at  $60 < Re_d < 180$  in a finite width channel by Stansby and Slaouti (1993) are consistent with this scaling.

The PE of the fluid relative to the fully mixed state is given by:

$$PE = -\rho_0 WL \int_0^H b(z') z' dz', \quad (2.5)$$

and the background PE change during the  $n$ th sequence of stirs is:

$$\overline{PE}_n = -\rho_0 WL \int_0^H \{b_n(z') - b_{n-1}(z')\} z' dz'. \quad (2.6)$$

Relations (2.4) and (2.6) are used to calculate the mixing efficiency from the experimental data. In addition, from Eqs. (2.2) and (2.5), it follows that:

$$\frac{\partial PE}{\partial t} = -\rho_0 WL \int_0^H q(z') dz'.$$

Writing:

$$\frac{\partial \text{KE}}{\partial t} = \rho_0 W L H E,$$

where  $E$  is the rate of KE input per unit mass, the mixing efficiency is then proportional to the depth-averaged buoyancy flux:

$$\eta = -\frac{1}{EH} \int_0^H q(z') dz'. \quad (2.7)$$

#### 2.4. Choice of external parameters

For definition of overall  $Re$  and  $Ri$ , values for  $N$  and the velocity and lengthscale of the turbulence appropriate to the whole flow are required. Since there are thin well-mixed layers at the top and bottom of the initial stratification, the gradient of the central, linearly stratified portion of the tank was used to give an initial buoyancy frequency  $N_0$ .

In considering the evolution of the mean buoyancy field, we assume the turbulence may be approximated by horizontally homogeneous turbulence with no mean flow. Although there is structure in the turbulence generated by each tow of the grid, this implies that over each sequence of stirs, there is no net inhomogeneity. This allows the use of a single turbulent velocity scale and lengthscale to represent the turbulence.

External velocity and lengthscales will be used, as measures of the imposed forcing of the fluid. There are two horizontal lengthscales, the bar thickness,  $d$ , and the mesh spacing,  $M$ . In unstratified turbulence generated by a biplanar grid, the turbulent lengthscale is proportional to the grid mesh length. We therefore expect  $M$  to be important at low  $Ri$ . The results of Section 3 confirm this lengthscale dependence and show that the velocity scale  $U_0 = U(1 - S)$ , used to estimate the drag on the rake Eq. (2.4), is again the most appropriate velocity scale, accounting for the effects of grid solidity. At higher  $Ri$ , we shall see that the dynamics of the vertical vorticity in the wake, contained in vortices of scale  $d$ , becomes important. The best collapse of data for critical  $Ri$ ,  $Ri_c$ , both for buoyancy effects in moderate stratification (Section 3), and for buoyancy control and layering (Section 4), is found using a lengthscale of  $L_0 = \sqrt{dM}$ .

The data were also scaled using the mesh length,  $M$ , and the bar width,  $d$ , as reference lengths. For reasons of space these plots are not presented but, in both cases, the collapse of the data is less convincing than with  $L_0$ . For the parameter values used in our experiments, both geometric features of the grid appear to be relevant and this is reflected in the use of  $L_0$ . In cases where both scales are not relevant, for example,  $M \gg d$  such as in the case of PWG94 where a single bar is used, then clearly  $d$  and not  $L_0$  is the relevant scale. The scaling we use seems appropriate when both grid scales are comparable, but will not extend to all grid geometries.

Using the scales  $L_0$  and  $U_0$ , the overall  $Re$  is defined by  $Re = U_0 L_0 / \nu$ , and the overall  $Ri_b$  for the ideal initial conditions by  $Ri_0 = N_0^2 L_0^2 / U_0^2$ . As the mean buoyancy profile evolves during each experiment, the buoyancy jump across the whole fluid depth,  $\Delta b$ , decreases. A time-evolving  $Ri_b$  is defined as  $Ri_b = \Delta b L_0^2 / H U_0^2$ , and will be used



to investigate variations in mixing during the course of an experiment. In all experiments,  $Ri_b$  decreases with time. A local  $Ri$  is defined as  $Ri(z,t) = N^2(z,t)L_0^2/U_0^2$ .

### 3. Evolution of the buoyancy field at low $Ri$

At low  $Ri_0$ , the density profiles remain smooth throughout the approach to a well-mixed state. Well-mixed boundary layers grow at the top and bottom of the fluid, where the turbulent buoyancy flux is blocked by the impermeable upper and lower boundaries. However, there is a smooth transition between these boundary layers and the interior. A typical sequence of buoyancy profiles is shown in Fig. 1, for an experiment with grid C (Table 1). In general, this kind of behaviour occurs for  $Ri_0 \leq 1.5$ , although at low  $Re < 400$  (obtained with grids A and B), layering occurs by a different mechanism for  $0.1 \leq Ri_0 \leq 1.5$ , as described by Holford and Linden (1999b). In this mechanism, layers develop by an essentially nonlocal analogue of the Phillips/Posmentier mechanism. Enhanced turbulence in well-mixed regions, such as the boundary layers, erodes the adjacent stratification causing an interface to develop. Such an interface then acts as a barrier to the transport of buoyancy out of the stratified interior, and a further well-mixed layer develops. The regime diagram in  $(Re, Ri_0)$  space is

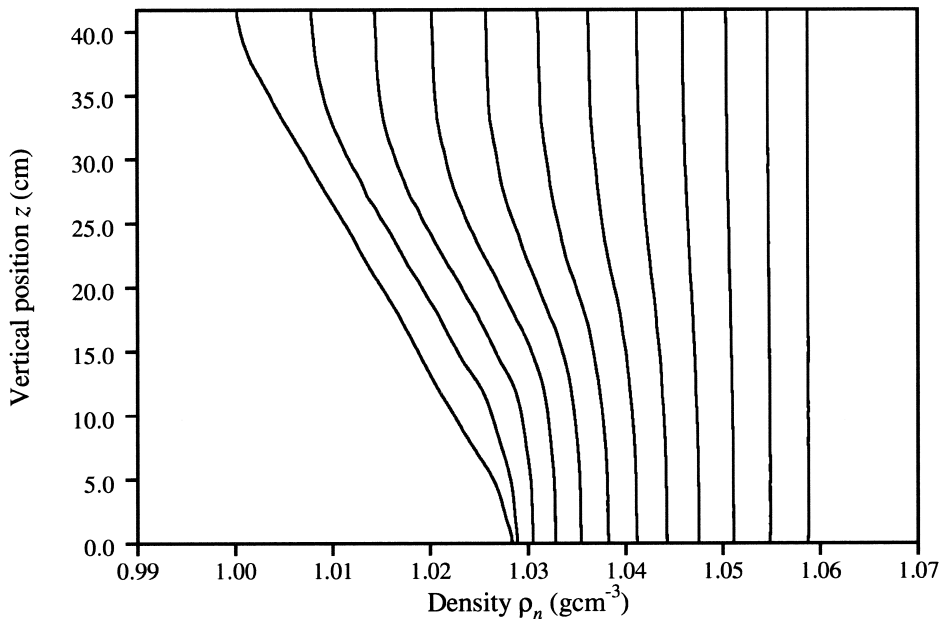


Fig. 1. The sequence of density profiles,  $\rho_n(z)$  for  $n=0,1,\dots,11$ , from experiment 123 with grid C at  $Ri_0 = 0.32$ . Each subsequent profile is shifted by  $0.004 \text{ g cm}^{-3}$ .

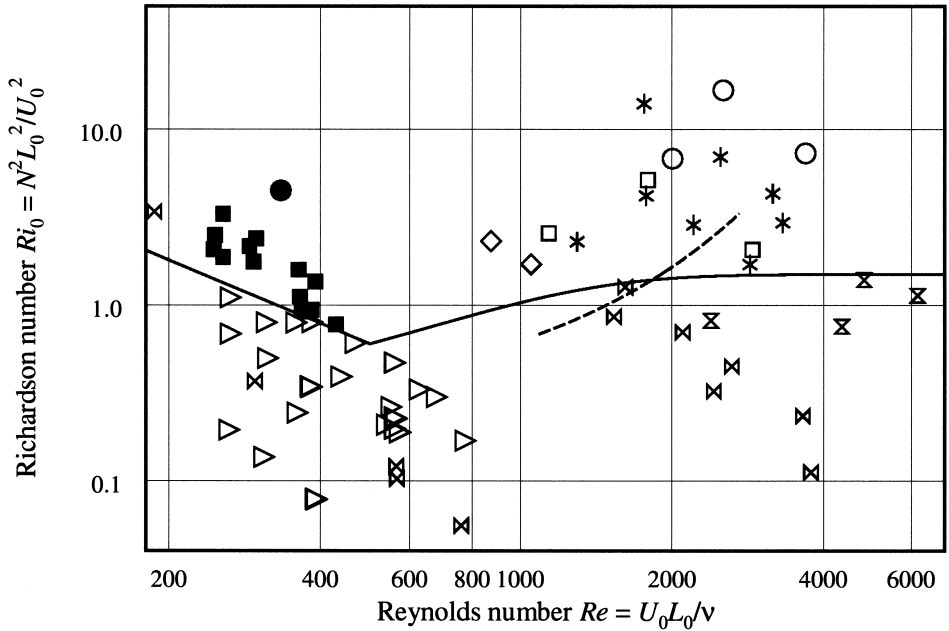


Fig. 2. A regime diagram showing the boundaries of different mixing behaviour in  $(Re, Ri_0)$  space. Experiments that develop layers through the mechanism discussed in this paper are shown by the symbols from Table 1. Experiments that develop layers by boundary mechanisms and from streamwise vortices in the wakes are shown as  $\triangleright$ , and experiments in which layers do not occur (with a range of grids) are shown as  $(\times)$  (DAMTP) and  $(\bar{\times})$  (EnFlo). The solid line is an approximation to the critical  $Ri_0$  for the mechanism discussed in this paper. The dashed line represents the layering boundary identified by PWG94, for a bar width  $d = 2.26$  cm in a tank of width  $M = 10$  cm. In terms of their parameters,  $Re_p = Ud/\nu = 0.368 Re$  and  $Ri_p = N^2 d^2 / U^2 = 0.377 Ri$ , the layering boundary is  $Ri_p = 0.09 \exp(Re_p / 380)$ , which agrees with the data in their Fig. 3, although not with their quoted function (3.1).

shown in Fig. 2, and the low  $Ri_0$  (nonlayering) experiments discussed in this section are shown as  $(\times)$  and  $(\bar{\times})$ .

### 3.1. Local behaviour

Density profiles are measured and processed as described in Section 2, to give profiles of  $N$  and  $q$ . Fig. 3a shows the relationship between  $q$  and  $N^2$  for the experiment shown in Fig. 1. All data from the discretised 0.1 cm profiles and all timesteps  $n \geq 2$  are plotted on this figure, and increasing greyscale intensity corresponds to increasing time. These data collapse very well, showing that  $q$  is a well-defined function of  $N^2$ , despite the presence of the upper and lower boundaries of the tank which will modify the turbulence field locally.

By extension of the diffusion of a passive scalar in an unstratified fluid, we assume a relationship of the form:

$$q = -K_b(N^2)N^2, \quad (3.1)$$

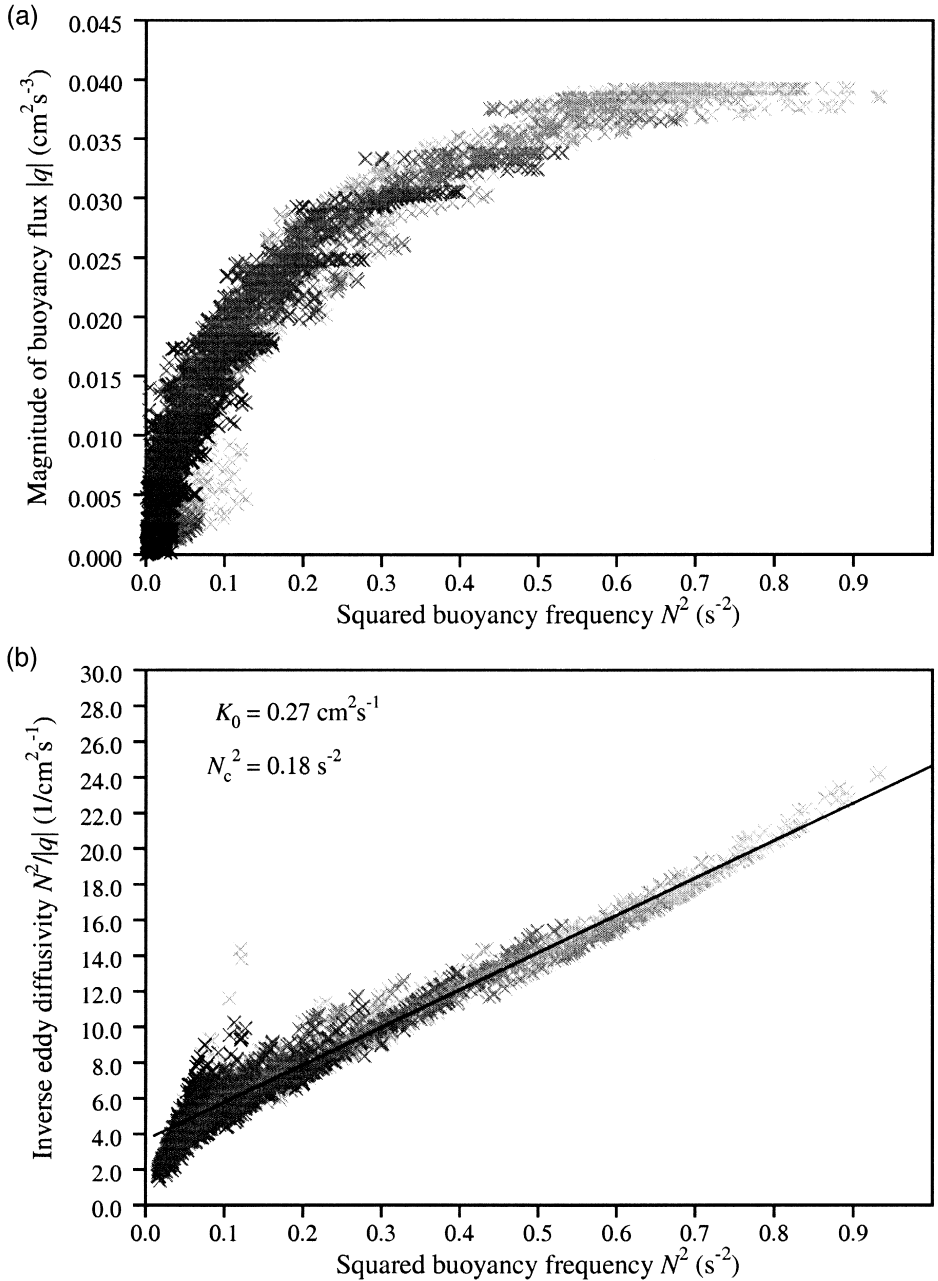


Fig. 3. The relationship between buoyancy flux and gradient in experiment 123 with grid C at  $Ri_0 = 0.32$  and  $Re = 2400$ , for sequences 2 to 11: (a) the magnitude of buoyancy flux  $|q|$  as a function of buoyancy gradient  $N^2$ , and (b) the same data, replotted as  $N^2/|q|$ , showing the least squares best-fit straight line to the data. This fitted form gives a correlation coefficient of 0.980. In both figures,  $|q_n|$  is compared to the average of the gradient at the start and end of sequence  $n$ ,  $(N_{n-1}^2 + N_n^2)/2$ , and darker symbols correspond to later times.

where  $K_b$  is the eddy diffusivity. In order to find  $K_b$ , we plot  $-N^2/q = 1/K_b$  against  $N^2$ , as shown in Fig. 3b. A straight line least squares fit to these data show that  $K_b$  is reasonably approximated by:

$$K_b = \frac{K_0}{(1 + N^2/N_c^2)}. \quad (3.2)$$

For weak stratifications, the eddy diffusivity is a constant  $K_b = K_0$ , whereas for stratifications  $N^2 \geq N_c^2$ , the diffusivity is significantly reduced below this level. In the limit  $N^2 \gg N_c^2$ , the buoyancy flux asymptotes to a constant value  $q = -K_0 N_c^2$ . However, as will be seen in Section 4, Eq. (3.1) is not valid at high  $Ri$ . We may compare Eq. (3.2) to the parametrisation chosen in the theoretical model of Noh and Fernando (1995):

$$K_b = e^{1/2} l_{\text{mix}} = \frac{e^{1/2} l_0}{\sqrt{1 + cN^2 l_0^2/e}}, \quad (3.3)$$

where  $e$  is the TKE,  $l_{\text{mix}}$  is the mixing length,  $l_0$  is the turbulent integral scale in an unstratified fluid, and  $c$  is a constant. Our empirical expression, Eq. (3.2), parametrises both the effect of a reduced mixing length, and of a reduction in TKE, as  $Ri$  increases.

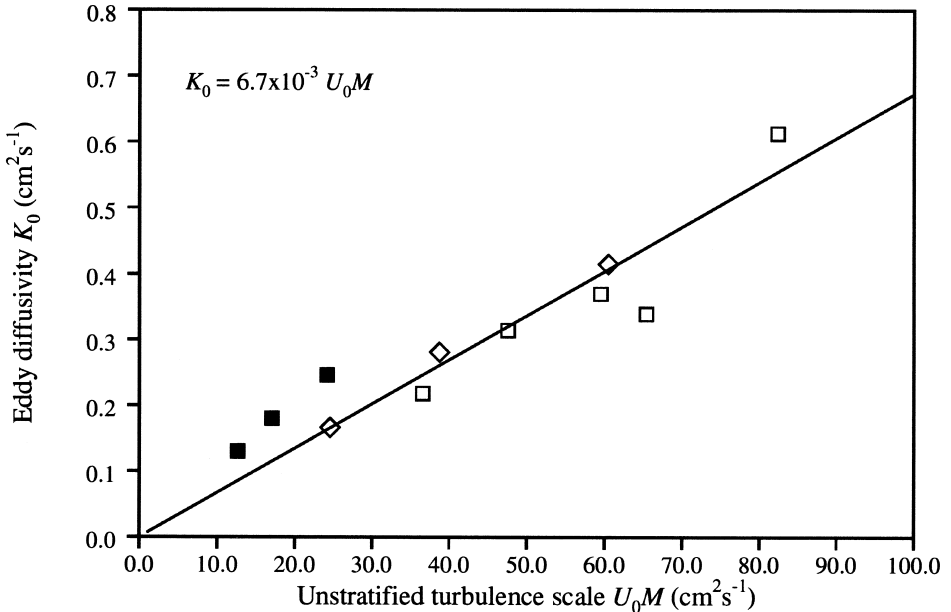


Fig. 4. Values of the eddy diffusivity  $K_0$  in the limit of zero stratification, as a function of  $U_0 M$ . Results from grids A, C and D are shown, with the symbols listed in Table 1, and the least squares best-fit linear relationship.

As  $Ri \rightarrow 0$ , Eq. (3.2) gives  $K_b = K_0$  while Eq. (3.3) gives  $K_b = e_0^{1/2} I_0$ , so the two parametrisations are equivalent and represent a constant eddy diffusivity. As  $Ri \rightarrow \infty$ , Eq. (3.2) gives  $K_b = K_0 N_c^2 / N^2$  and hence  $q = -K_0 N_c^2$ , while Eq. (3.3) gives  $K_b = e_\infty / c^{1/2} N$  and hence  $q = -e_\infty N / c^{1/2}$ , so the two parametrisations are equivalent only if  $e_\infty = c^{1/2} K_0 N_c^2 / N$ .

It is expected that  $K_0$  and  $N_c^2$  depend on the characteristics of the turbulence, and therefore on the external scales  $U$ ,  $d$  and  $M$ . Data were taken from 11 experiments in the range  $Ri_0 \leq 1.5$ , and the eddy diffusivity calculated from each. The coefficient  $K_0$  was found to depend on the mesh length  $M$ , as well as the velocity scale  $U_0$ , as shown in Fig. 4. For all experiments,  $K_0 = 6.7 \times 10^{-3} U_0 M$ .

The critical stratification  $N_c^2$  at which buoyancy effects become important can be expressed in terms of a critical  $Ri$ ,  $Ri_c = N_c^2 L_0^2 / U_0^2$ , so that:

$$K_b = \frac{K_0}{(1 + Ri/Ri_c)}. \quad (3.4)$$

For experiments with grids C and D,  $Ri_c = 0.065$ . However, for experiments with the grid A, the smallest grid, and consequently the lowest  $Re$ , stratification affected the flow at a lower  $Ri_c = 0.01$ . At these low  $Re$ , turbulence develops in the wake of the rake from 3D instabilities of the Kármán vortex street, whereas at higher  $Re$ , the Kármán vortices are turbulent on formation. The differences in the value of  $Ri_c$  suggest that the

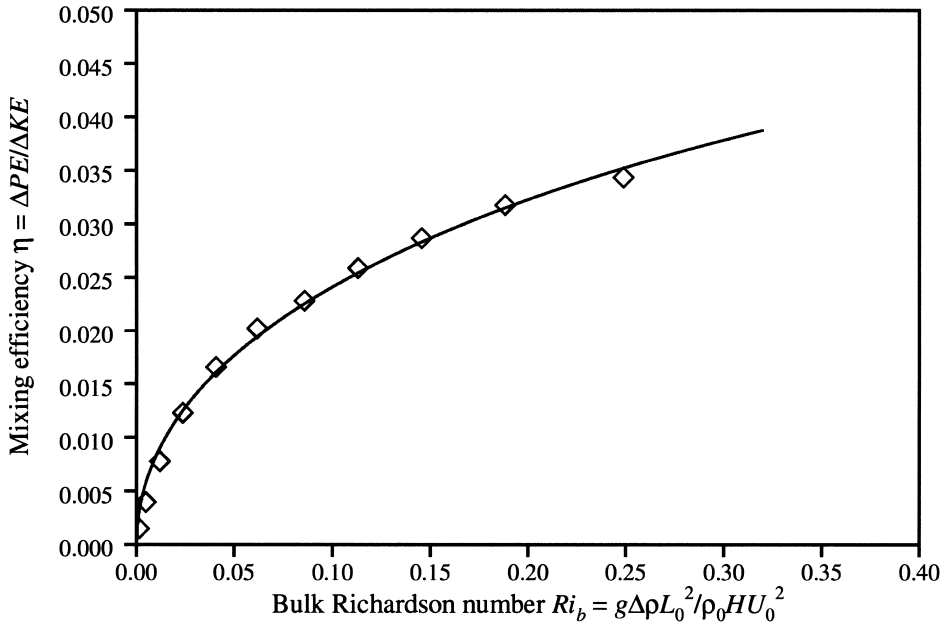


Fig. 5. Evolution of the mixing efficiency  $\eta$  with  $Ri_b$ , for experiment 123 ( $Ri_0 = 0.32$  and  $Re = 2400$ ), showing the extrapolation (based on an empirical functional form  $\eta = aRi_0^{1/2} + bRi_0$ ) back to a value of  $\eta_0 = 0.039$  at  $Ri_0 = 0.32$ .

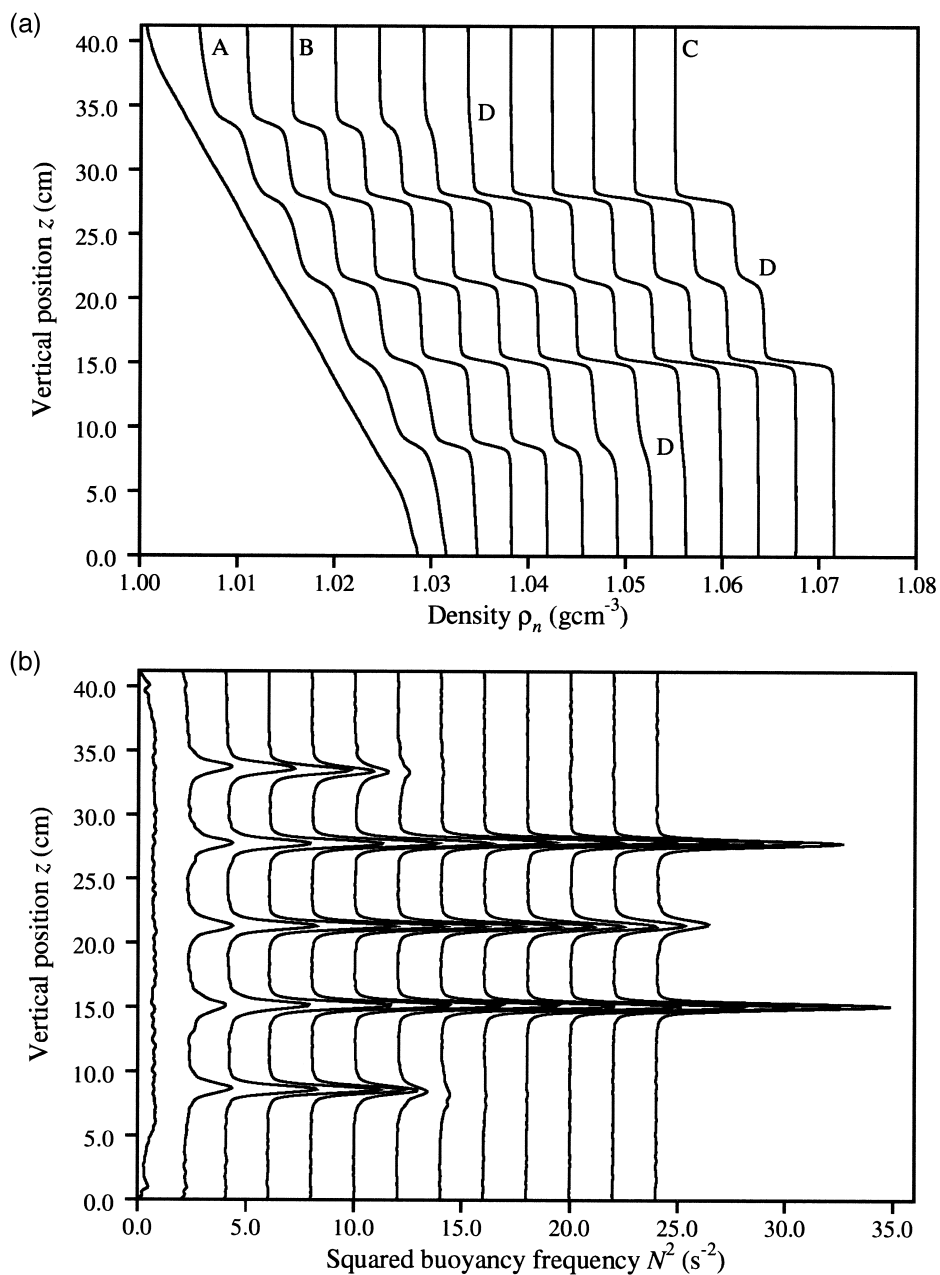


Fig. 6. The evolution of experiment 125 with grid C at  $Ri_0 = 1.72$ ,  $Re = 1050$ : (a) the sequence of density profiles,  $\rho_n(z)$ , each subsequent profile shifted by  $0.004 \text{ g cm}^{-3}$ , and (b) the sequence of buoyancy frequency profiles,  $N_n^2(z)$ , each subsequent profile shifted by  $2.0 \text{ s}^{-2}$ , for  $n = 0, 2, \dots, 24$ .

effect of stratification is more significant in suppressing the 3D instabilities at low  $Re$  than in damping existing turbulence structures at higher  $Re$ . With grid A, previously unobserved layering behaviour occurred for  $0.1 \lesssim Ri_0 \lesssim 1.5$ , which is discussed in Holford and Linden (1999b). For  $Ri_0 \geq 1.5$ , the evolution of the flow with grid A was investigated by Holford and Linden (1999a), and will be discussed in Section 4.

### 3.2. Global behaviour

The mixing efficiency  $\eta$  decreases in all experiments almost linearly with time. Alternatively, the evolution of the experiment can be followed on a plot of  $\eta(t)$  against the  $Ri_b(t)$ , as shown in Fig. 5. As the experiment progresses, both  $Ri_b(t) \rightarrow 0$  and  $\eta(t) \rightarrow 0$  as  $t \rightarrow \infty$ . As the well-mixed boundary layers grow, a greater fraction of the fluid depth is only weakly stratified. Since the buoyancy flux  $q$  is an increasing function of  $N^2$ , the boundary layers support a smaller flux than the stratified interior. Hence the depth-averaged buoyancy flux and, from Eq. (2.7),  $\eta$  decrease as the boundary layers grow.

## 4. Evolution of the buoyancy field at high $Ri$

At high  $Ri_0$ , the evolving density profile no longer remains smooth, but develops a series of interfaces and layers. A time sequence of density profiles from a typical

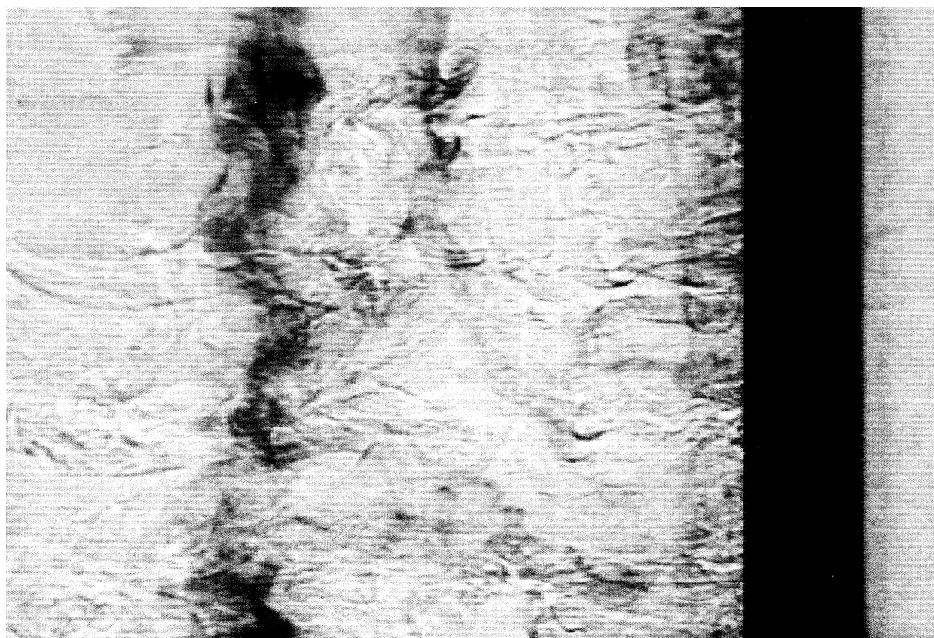


Fig. 7. An enhanced shadowgraph of the wake behind grid C during the first stirring sequence of experiment 125. The rake, in black, is moving from left to right, and a dark powder is released from one side of one of the bars, marking a vortex core.

layering experiment with grid C is shown in Fig. 6a, and the associated buoyancy frequency profiles are shown in Fig. 6b. The layering develops across the whole tank depth at the same rate, and with a regular vertical scale.

Layering at this  $Ri_0$  with grid A was investigated by Holford and Linden (1999a), as discussed in the introduction. The important result of this work is that similar dynamics is observed at these high  $Ri_0$ , even with grid configurations for which  $Re$  is much higher. Fig. 7 is a shadowgraph of the wake behind grid C, at  $Re = 1050$ , with a powder dye streak marking a distorted vortex core. Even with grid F, at the largest  $Re = 3300$ , a streak of dye shed from a bar during layering remained coherent, and developed the same form of vertical perturbations. A vortex street pattern is observed behind a circular cylinder up to  $Re_d \approx 3 \times 10^5$  (Tritton (1988)), although for  $Re_d \geq 400$  the vortices are turbulent at their formation. Our observations show that stratification maintains this vortical component of the flow, and damps turbulent motions, so the vertical vorticity dominates the evolution at early times.

Further confirmation that the layering process is similar for all six grids and  $Re$  is given by the scale of the layers that form, shown in Fig. 8 as a function of the buoyancy scale  $U/N$ . There is excellent collapse of the data, with a best fit relation  $l = 3.07U/N$ . Here, the relevant velocity scale is the grid velocity  $U$  rather than the relative velocity  $U_0$ , because the layering is related to the vertical vorticity and hence the wake instability process, which is insensitive to the mesh spacing, rather than the general characteristics of the turbulence. The layer scale observed by PWG94, at comparable  $Ri_0$ , was

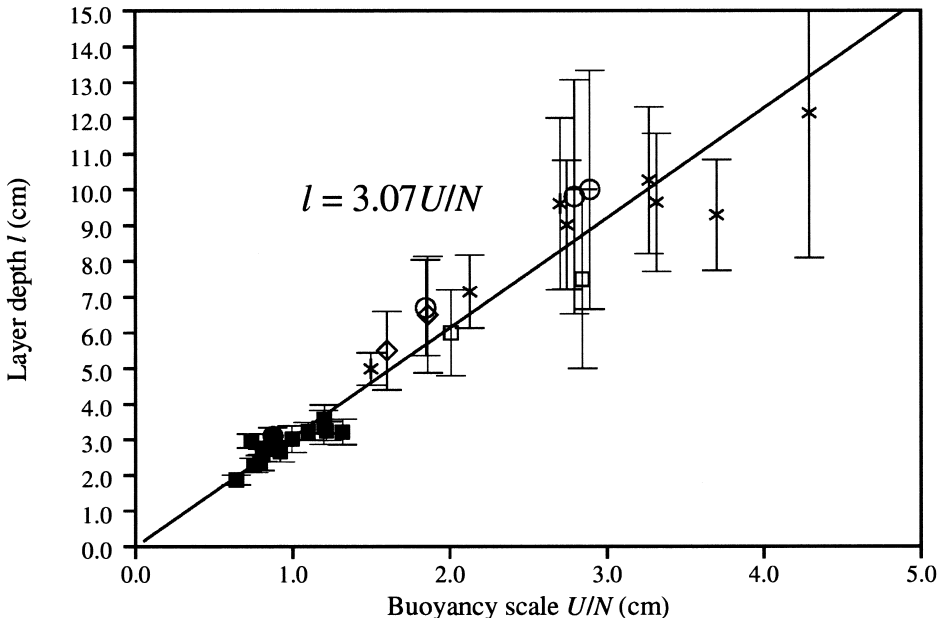


Fig. 8. The scale of layers  $l$  produced by all grids in these experiments, as a function of the buoyancy lengthscale  $U/N$ , showing the least squares best-fit linear relationship. Data from all six grids are included, represented by the symbols given in Table 1. The error bars are determined by the constraint that there is always an integer number of layers in the fluid depth.



$l = 2.6U/N + 1.0$  cm, and the similarity of scale suggests that the same generation mechanism may be responsible. It is clear that, as in previous layering experiments, the layer thickness is much larger than the buoyancy scale  $L_b = w/N$ , where  $w$  is the vertical turbulent velocity scale, which is significantly less than  $U/N$ .  $L_b$  is a measure of the maximum vertical turbulent lengthscale in a stratified fluid (Britter et al., 1983).

Returning to Fig. 6, it can be seen that the positions of interfaces do not alter significantly with time, even from the early stage of sequence 2 (marked A). By sequence 6 (B), five interfaces are present with an approximately equal buoyancy jump across each. The outer interfaces quickly decay, leaving three interfaces; then the central interface begins to decay, and at the end of the experiment (C) the fluid is approaching a three-layer structure. The positions of decaying interfaces are marked by D. The processes of layer development and decay are discussed further in Section 4.1.

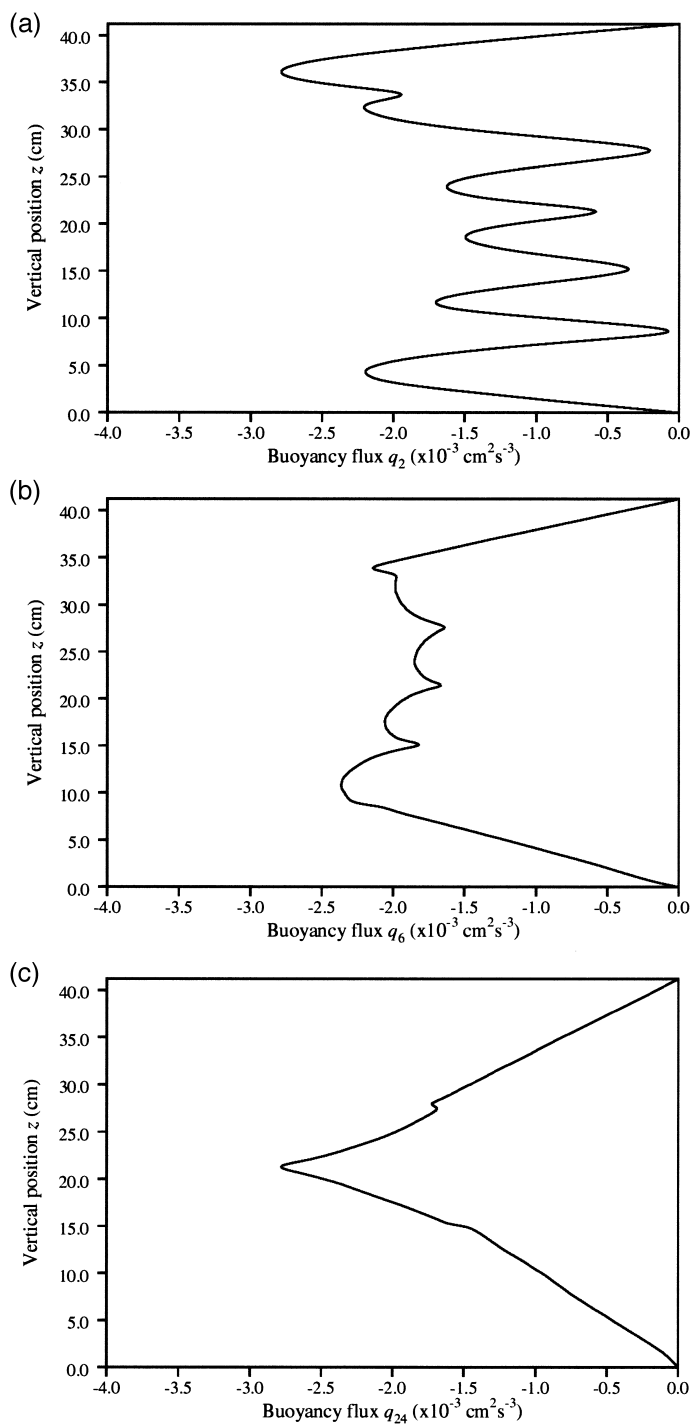
#### 4.1. Local behaviour

Profiles of  $q_n$  calculated for a high  $Ri_0$  experiment, corresponding to the three sequences  $n = 2, 6$  and  $24$  are shown in Fig. 9a, b and c. During sequence 2,  $q_2$  takes very low values at the positions of the developing interfaces. There are large divergences of flux, indicative of the developing structure, as the fluid is mixed up within each layer. By the end of sequence 6,  $q_6$  is more uniform in the interior, and decreases linearly to zero in the well-mixed boundary layers. The uniformity of  $|q|$  shows that the fluid is, at this time, in a quasi-steady state. The subsequent decay of interfaces is not quasi-steady, and the decaying central interface in sequence 24 is marked by a local maximum of  $|q_{24}|$ .

Fig. 10 shows the relationship between  $q$  and  $N^2$  at the beginning and end of the experiment, at sequences  $n = 2$  and  $24$ . There is now no direct  $q(N^2)$  relationship equivalent to that in Fig. 3 at low  $Ri_0$ , and the overall patterns are qualitatively different between the two times.

Insight into the layer development is gained by identifying the layers and interfaces in each profile, by the minima and maxima of  $N^2$ , respectively, and following the buoyancy flux at these points alone, as in Fig. 11. On this figure, the broken line styles corresponds to an interface, while the solid linestyles corresponds to layers. Fig. 11a displays the whole range of behaviour, and Fig. 11b is an enlargement of the weakly stratified range. Initially, the buoyancy frequency is everywhere approximately the initial value,  $N^2 = 0.74 \text{ s}^{-2}$ . However, as discussed in Section 2.2, the density profile extrapolation to the boundaries is relatively unsuccessful for the initial profile, and consistent flux measurements can only be calculated from the second stirring sequence, by which time the interfaces have  $N^2 \approx 1.6 \text{ s}^{-2}$  and the layers have  $N^2 \approx 0.5 \text{ s}^{-2}$ . The buoyancy flux is larger at the positions where the layers are developing than at the interfaces. This divergence of buoyancy flux leads to the development of a strong layered structure.

Within the layers,  $N^2$  decreases monotonically with time, and  $q$  first increases and then rapidly falls in the manner of the weakly stratified  $q(N^2)$  relationship discussed in Section 3.1, shown in Fig. 11 as the solid heavy line. At the developing interfaces,  $N^2$  increases and  $q$  also increases. Then, once each interface is well-defined, a relationship



in which  $q$  is a decreasing function of  $N^2$  is observed, sketched on Fig. 11 as the dashed heavy line. Therefore, as an interface continues to strengthen (dotted lines),  $N^2$  rises and  $q$  falls, whereas when an interface decays,  $N^2$  falls and  $q$  rises (dashed lines). The high values of  $q$  at decaying interfaces were noted by PWG94, who explained these values in terms of the postulated Phillips/Posmentier relationship. Here we see that the decay of an interface is clearly not just the reverse of formation, as  $q$  continues to rise to the maximum value observed in the experiments, before finally falling on the diffusive  $q(N^2)$  relationship. This difference between formation and decay occurs because the turbulence has a different structure in the two situations.

The details of the early stages of the layering process are different to that exhibited in the moderate  $Ri_0$  layering observed, at lower  $Re$ , by Holford and Linden (1999b). In the present experiments, layers develop more quickly, as the divergence of the flux is more significant, with initially significantly higher flux within the layers than at the interfaces. Also, the layering proceeds uniformly throughout the fluid depth, and so there is good collapse of the  $q(N^2)$  separately for well-developed layers and for interfaces, as seen in Fig. 11. However, when the layered structure is well-developed,  $q$  falls as  $N^2$  rises at the interfaces in both layering regimes, as is observed in mixing box studies, and in the layering experiments of PWG94.

#### 4.2. Global behaviour

The variation of mixing efficiency  $\eta$  with  $Ri_b$  in a high  $Ri_0$  experiment is shown in Fig. 12. Rather than the smooth reduction in  $\eta$  with time observed in low  $Ri_0$  experiments, such as that shown in Fig. 5,  $\eta$  rises and falls about an overall decreasing trend. In general,  $\eta$  falls as all the interfaces strengthen, and rises when one or more of the interfaces decay. The decay of an interface is associated with an increase in buoyancy flux, which can lead to an increase in the depth-averaged buoyancy flux and hence, from Eq. (2.7), in  $\eta$ .

### 5. Variation of initial mixing efficiency with $Ri$

We have seen from Eq. (2.7), that the mixing efficiency  $\eta$  depends upon the structure present in the density profile, as this structure can alter the depth-averaged buoyancy flux. Therefore, for a meaningful investigation of  $\eta$  variation with  $Ri$ , measurements of  $\eta$  must be made in flows with similar structure. In the initial conditions in these experiments, boundary layers of nonzero thickness are present, so we extrapolate the measured  $\eta$  back to its value  $\eta_0$  at  $Ri_0$  corresponding to the ideal linear initial stratification. A typical extrapolation for a low  $Ri_0$  experiment is shown in Fig. 5. For experiments at higher  $Ri_0$ , in which layering occurs,  $\eta$  is sensitive to the precise

---

Fig. 9. Three buoyancy flux profiles from experiment 125: (a)  $q_2$ , as the layered structure forms, (b)  $q_6$ , when five similar interfaces are present, and (c)  $q_{24}$ , as the central interface of three weakens.

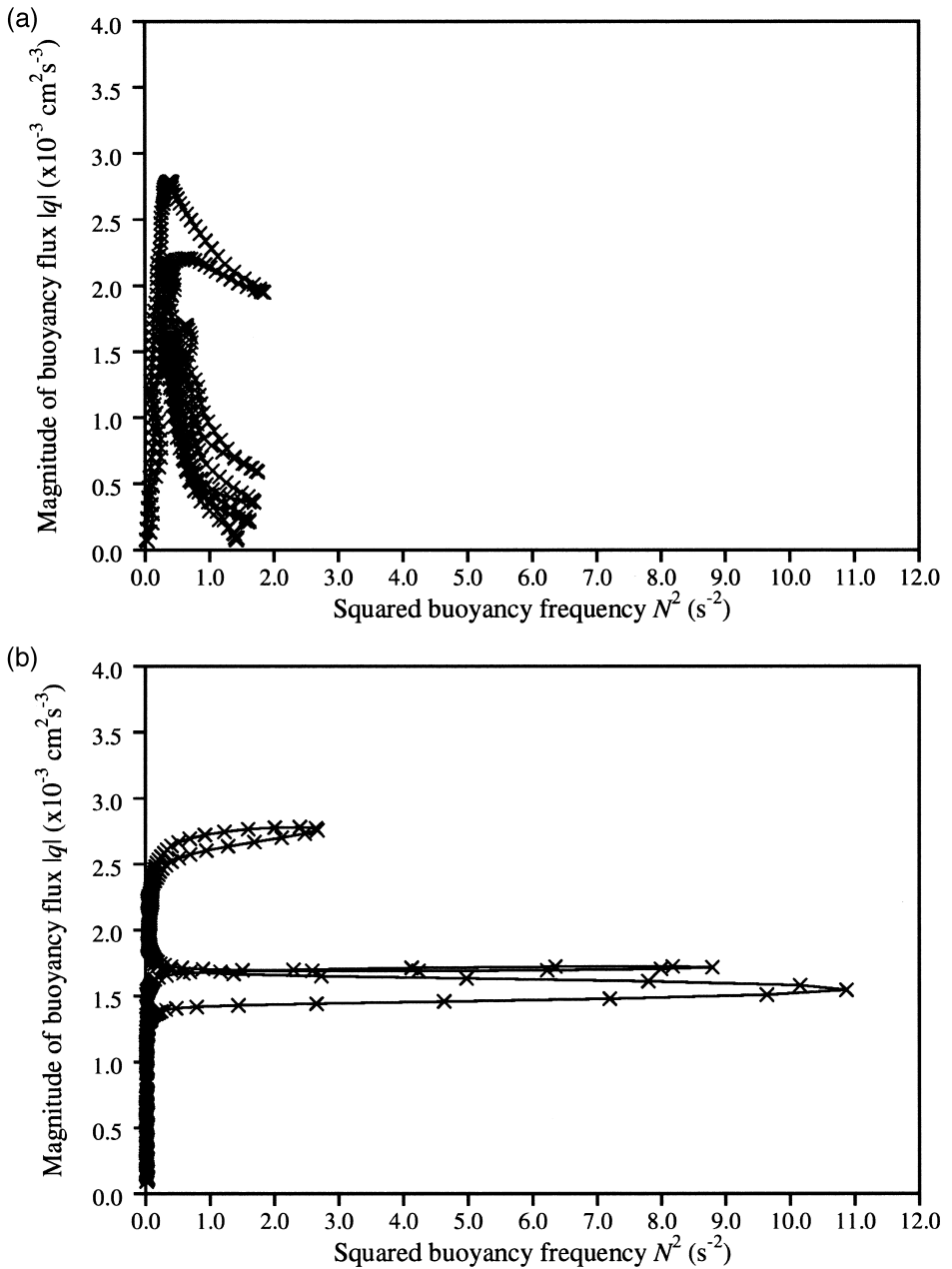


Fig. 10. The relationship between the magnitude of buoyancy flux  $|q|$  and buoyancy gradient  $N^2$  in experiment 125 at two stages: (a)  $n=2$  as the layered structure forms, and (b)  $n=24$ , when three interfaces are present. Again,  $|q_n|$  is shown as a function of  $(N_{n-1}^2 + N_n^2)/2$ .

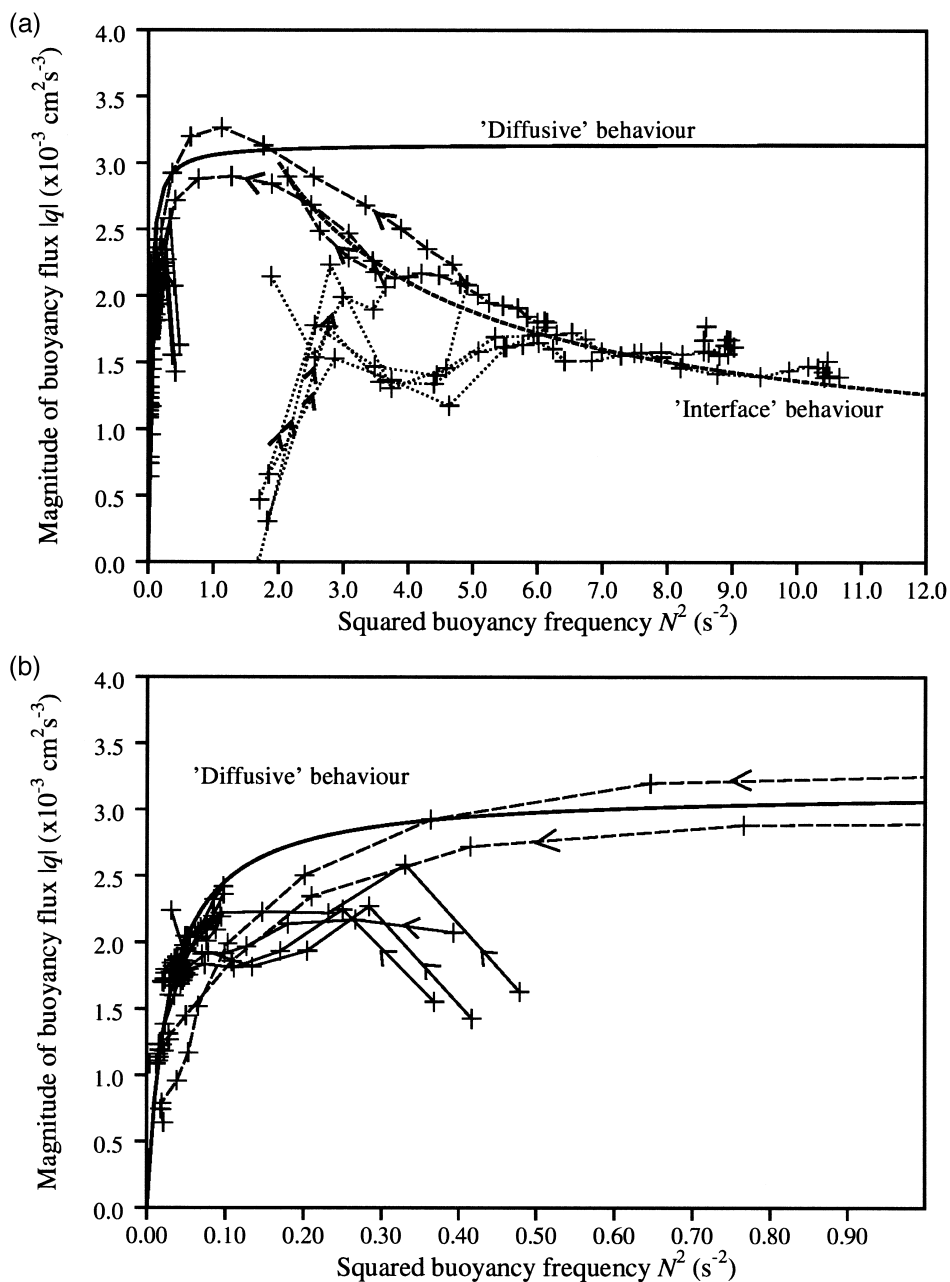


Fig. 11. The relationship between buoyancy flux  $|q|$  and buoyancy gradient  $N^2$  in experiment 125 ( $N_0^2 = 0.74 \text{ s}^{-2}$ ) at selected vertical positions, during the entire experiment. Four layers (solid lines) and five interfaces (dotted lines while strengthening, dashed lines while decaying) are shown, and the arrows indicate time evolution. (a) shows the whole range of behaviour, and (b) is an enlargement of  $N^2 < 1 \text{ s}^{-2}$ , to show more detail in this range. The heavy solid line is diffusive behaviour predicted from the lower  $Ri_0$  experiments, and the heavy dashed line is a sketch of the behaviour of well-developed interfaces.

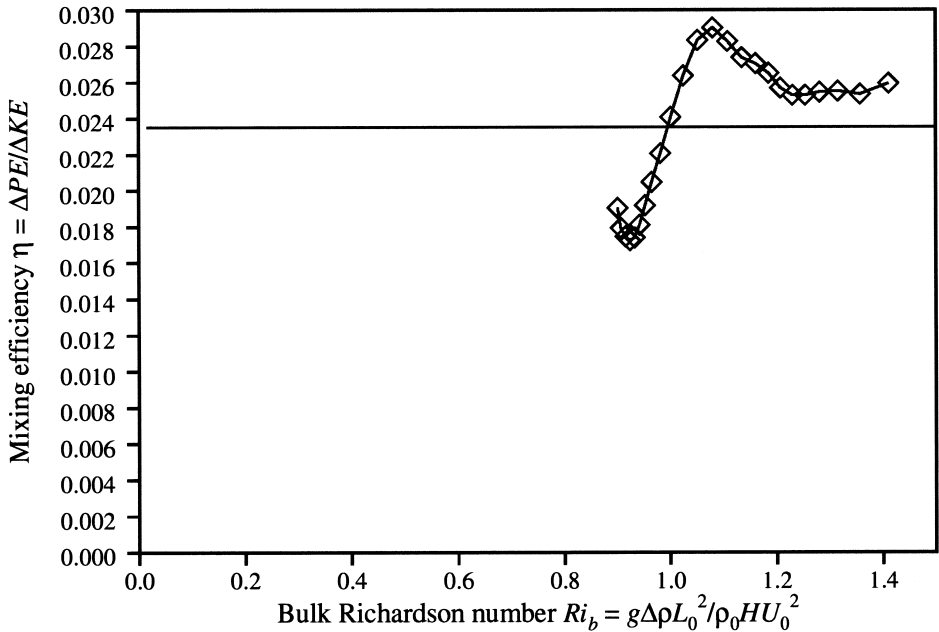


Fig. 12. Evolution of the mixing efficiency  $\eta$  with  $Ri_b$ , for experiment 125. Here the average value (solid line) is used to estimate  $\eta_0 = 0.024$  at  $Ri_0 = 1.72$ .

dynamics of the interfaces, and a time average value for  $\eta_0$  is taken, as shown in Fig. 12.

The resulting  $\eta_0$  from experiments using grids A, C and D are plotted against  $Ri_0$  in Fig. 13. For  $Ri_0 \leq 1.5$ , when layering does not occur, the scaling used collapses the data for  $\eta_0$  with grids C and D onto an increasing curve. For grid A, values for  $\eta_0$  at  $Ri_0 \leq 0.3$  follow the same scaling, but above this threshold, layers develop by a separate mechanism, as discussed in Section 3.1, and as a result  $\eta_0$  is lower. For  $Ri_0 \geq 1.5$ , in the layering regime,  $\eta$  decreases for grids C and D as  $Ri_0$  increases, but falls more rapidly for grid C, which has the higher solidity. The more solid grid generates more vortices per unit area, and so requires a different scaling in the high  $Ri_0$  regime. These experiments demonstrate a maximum in  $\eta_0$  at a critical  $Ri_0$ , as observed in the experiments on mixing across interfaces by Linden (1980).

The maximum value of the  $\eta_0$  measured is around 0.05, which is comparable with values from some other experiments, including Huq and Britter (1995) and PWG94. These values are low compared to values for the maximum flux Richardson number,  $Rf \approx 0.15$ – $0.25$  in shear-driven mixing suggested by turbulence closure theories (e.g., Ellison, 1957), by oceanographic measurements (e.g., Peters and Greggs, 1988), and by laboratory experiments (e.g., Rohr et al., 1984). It is possible that the observed low values of  $\eta$ , which is proportional to the spatial average of  $q$ , reflect the spatial and temporal intermittency of regions of the peak  $q$ . In addition, the ratio of  $q$  to viscous dissipation, which is represented by  $Rf$ , may be sensitive to the nature of the mixing

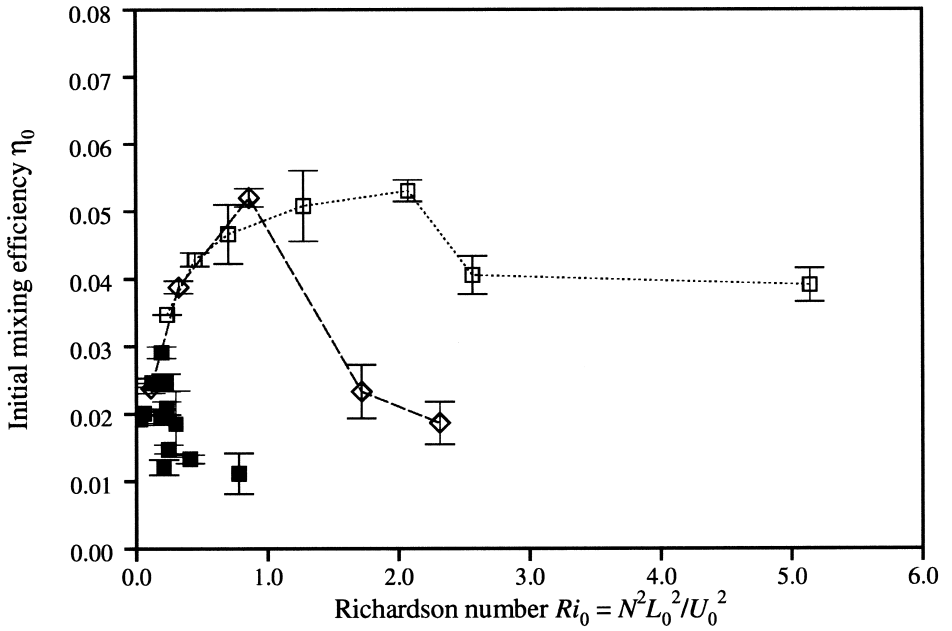


Fig. 13. The variation in mixing efficiency  $\eta_0$  at the ideal initial  $Ri$ ,  $Ri_0$  for experiments with grids A, C and D, displayed using the symbols from Table 1, showing the peak at the boundary between layering and nonlayering regimes for grids C and D. In experiments with grid A at  $Ri_0 > 0.8$ ,  $\eta_0$  was too small to be resolved with the current measuring system.

process, resulting in a lower value of  $Rf$  for this mechanical mixing than for the shear-driven mixing.

## 6. Conclusions

The primary conclusion of this work is that the layering observed is not a result of the Phillips/Posmentier mechanism. At high values of the overall  $Ri$ ,  $Ri_0$ , the regions of vertical vorticity dominate the flow evolution, and cause the formation of a layered structure in the density profile through an interaction between the vortices and stratification. The ubiquity of this dynamical behaviour for several grid geometries, and over a wide range of  $500 < Re < 4000$ , has been shown, with a well-defined layer scale of  $l = 3.07U/N$ .

In low  $Ri_0$  flows, we have measured a  $Ri$ -dependent eddy diffusivity which represents the relationship between buoyancy flux  $q$  and local  $Ri$ . In the limit as  $Ri \rightarrow 0$ , the eddy diffusivity approaches a constant value of  $K_0 = 6.7 \times 10^{-3} U_0 M$ . The  $Ri$  at which the stratification first begins to affect the flow is a constant for larger grids,  $Ri_c \approx 0.065$ , and the reduction in the eddy diffusivity is given by Eq. (3.4).

The buoyancy flux profiles taken in high  $Ri_0$  layered flows show that at fully developed and decaying the interfaces, the flux is governed by a relationship similar to

that observed in mixing box experiments, in that the flux decreases with increasing buoyancy gradient. Within the layers, the flux approaches the value given by the diffusive relationship measured in low  $Ri_0$  flows. In contrast, where the vortex cores remain vertical and the layers first develop, the flux is less than predicted by either the layer or interface relationships. Although there is a well-defined relationship between buoyancy flux and gradient once the layered structure is formed, this is not the case during the development of layers, which cannot therefore be a result of the Phillips/Posmentier instability.

The model of Balmforth et al. (1997) predicts an  $N$ -shaped  $q(N^2)$  relationship at the equilibrium TKE distribution. In the initial stages of the present experiments, the  $q(N^2)$  relationship takes approximately this form, see Fig. 11, but it is not an equilibrium relationship and, as the interfaces sharpen,  $q$  decreases with further increases in  $N^2$ . Once the layered structure has developed there is a well-defined  $q(N^2)$  relationship with a maximum in that experiment at  $N^2 \approx 1 \text{ s}^{-2}$ . This relationship is of the form assumed in the Phillips/Posmentier model, but does not hold in our experiments in the initial stages when there is less structure in the profile. Hence, we see that the peaked  $q(N^2)$  relationship is a result of the layering, rather than an explanation for its development.

For all but the lowest  $Re$  flows, the initial mixing efficiency is shown to reach a maximum value of  $\eta_0 \approx 0.05$  at  $Ri_0 \approx 1.5$ , which corresponds to the boundary between diffusive and layering behaviour. Below this critical  $Ri_0$ , the mixing efficiency is independent of grid geometry, whereas at larger  $Ri_0$ , it varies with the grid solidity. As the layered structure develops, the mixing efficiency reduces still further, although decaying interfaces can lead to an increase in mixing efficiency. Therefore, we see that the structure of the stratification, as well as an overall  $Ri$ , affects the amount of mixing, as measured by the mixing efficiency.

Although these experiments use a specialised stirring mechanism, we believe that the control of local mixing by the pattern of vertical vorticity may be important in many high  $Ri$  flows, where this vorticity component is a dominant feature. Oceanographic and atmospheric motions show that much of the kinetic energy resides in mesoscale eddies which are characterised by large values of the vertical vorticity. As eddies ‘slide’ over one another dissipation occurs (see Fincham et al. (1994)). Also vortex lines are tilted as in these experiments. Our results suggest this may be a mechanism that leads to layer formation.

We have also shown that in these experiments, the variation of mixing efficiency with an overall  $Ri_0$  has no simple relation to the local flux/gradient relationship when the structure of the flow is evolving and changing. Therefore, observational measurements of buoyancy flux averaged over regions of evolving structure may give complex results. Parametrisations may need to take account of the evolution of the local profile as well as instantaneous gradients.

## Acknowledgements

The authors would like to thank all those at the Environmental Flow Research Laboratory, at the University of Surrey, and especially the technician Mr. Tom Lawton,



for their support of this project. In addition, we would like to thank the technical staff Mr. David Page-Croft, Mr. Brian Dean, Mr. David Lipman and Mr. Caspar Williams for assistance with the laboratory work at DAMTP. This work was supported by the NERC under research grant GR3/8891.

## References

- Balmforth, N.J., Llewellyn Smith, S.G., Young, W.R., 1997. Dynamics of interfaces and layers in a stratified turbulent fluid. *J. Fluid Mech.* 355, 329–358.
- Barenblatt, G.I., Bertsch, M., Dal Passo, R., Prostokishin, V.M., Ughi, K., 1993. A mathematical model of turbulent heat and mass transfer in stably stratified shear flow. *J. Fluid Mech.* 253, 341–358.
- Batchelor, G.K., 1949. Diffusion in a field of homogeneous turbulence: I. Eulerian analysis. *Aust. J. Sci. Res.* 2, 437–450.
- Britter, R.E., Hunt, J.C.R., Marsh, G.L., Snyder, W.H., 1983. The effects of stable stratification on turbulent diffusion and the decay of grid turbulence. *J. Fluid Mech.* 127, 27–44.
- Dalaudier, F., Sidi, C., Crochet, M., Vernin, J., 1994. Direct evidence of ‘sheets’ in the atmospheric temperature field. *J. Atmos. Sci.* 51, 237–248.
- Davis, R.W., Moore, E.F., 1982. A numerical study of vortex shedding from rectangles. *J. Fluid Mech.* 116, 475–506.
- Ellison, T.H., 1957. Turbulent transport of heat and momentum from an infinite rough plane. *J. Fluid Mech.* 2, 456–466.
- Fernando, H.J.S., 1991. Turbulent mixing in stratified fluids. *Annu. Rev. Fluid Mech.* 23, 455–493.
- Fincham, A.M., Maxworthy, T., Spedding, G.R., 1994. Energy dissipation and vortex structure in freely decaying, stratified grid turbulence. *Dyn. Atmos. Oceans* 23, 155–169.
- Holford, J.M., Linden, P.F., 1999a. The development of layers in a stratified fluid. *Mixing and Dispersion in Stably Stratified Flows*. Proc. of 5th IMA Conf. on Stratified Flows. Oxford Univ. Press, pp. 165–179.
- Holford, J.M., Linden, P.F., 1999b. Boundary-driven layering in a turbulent stratified flow. *Phys. Fluids*, submitted.
- Huq, P., Britter, R.E., 1995. Turbulence evolution and mixing in a two-layer stably stratified fluid. *J. Fluid Mech.* 285, 41–67.
- Linden, P.F., 1979. Mixing in stratified fluids. *Geophys. Astrophys. Fluid Dyn.* 13, 3–23.
- Linden, P.F., 1980. Mixing across a density interface produced by grid turbulence. *J. Fluid Mech.* 100, 691–703.
- Liu, H.-T., 1995. Energetics of grid turbulence in a stably stratified fluid. *J. Fluid Mech.* 296, 127–157.
- Majda, A.J., Grote, M.J., 1997. Model dynamics and vertical collapse in decaying strongly stratified flows. *Phys. Fluids* 9, 2932–2940.
- Miyazaki, T., Fukumoto, Y., 1992. Three-dimensional instability of strained vortices in a stably stratified fluid. *Phys. Fluids A* 4, 2515–2522.
- Noh, Y., Fernando, H.J.S., 1995. Onset of stratification in a mixed layer subjected to a stabilizing buoyancy flux. *J. Fluid Mech.* 304, 27–46.
- Park, Y.-G., Whitehead, J.A., Gnanadesikan, A., 1994. Turbulent mixing in stratified fluids: layer formation and energetics. *J. Fluid Mech.* 279, 279–311.
- Peters, H., Greggs, M.C., 1988. On the parametrization of equatorial turbulence. *J. Geophys. Res.* 93, 1199–1218.
- Phillips, O.M., 1972. Turbulence in a strongly stratified fluid — is it unstable?. *Deep-Sea Res.* 19, 79–81.
- Posmentier, E.S., 1977. The generation of salinity finestructure by vertical diffusion. *J. Phys. Oceanogr.* 7, 298–300.
- Rohr, J.J., Itsweire, E.C., van Atta, C.W., 1984. Mixing efficiency in stably stratified decaying turbulence. *Geophys. Astrophys. Fluid Dyn.* 29, 221–236.
- Ruddick, B.R., McDougall, T.J., Turner, J.S., 1989. The formation of layers in a uniformly stirred density gradient. *Deep-Sea Res.* 36, 597–609.

- Stansby, P.K., Slaouti, A., 1993. Simulation of vortex shedding including blockage by the random-vortex and other methods. *Int. J. Numer. Methods Fluids* 17, 1003–1013.
- Stillinger, D.C., Helland, K.N., van Atta, C.W., 1983. Experiments on the transition of homogeneous turbulence to internal waves in a stratified fluid. *J. Fluid Mech.* 131, 91–122.
- Taylor, G.I., 1915. Eddy motion in the atmosphere. *Philos. Trans. R. Soc. London* 215A, 1–26.
- Tritton, D.J., 1988. *Physical Fluid Dynamics*. Oxford Science Publications, 519 pp.
- Turner, J.S., 1968. The influence of molecular diffusivity on turbulent entrainment across a density interface. *J. Fluid Mech.* 33, 639–656.
- Turner, J.S., 1973. *Buoyancy Effects in Fluids*. Cambridge Univ. Press, 367 pp.
- Winters, K.B., Lombard, P.N., Riley, J.J., D’Asaro, E.A., 1995. Available potential energy and mixing in density-stratified fluids. *J. Fluid Mech.* 289, 115–128.